

Photodynamics and ground state librational states of ClF molecule in solid Ar. Comparison of experiment and theory

Toni Kiljunen,^a Matias Bargheer,^{†a} Markus Gühr,^a Nikolaus Schwentner^a and Burkhard Schmidt^b

^a Institut für Experimentalphysik, Freie Universität Berlin, Arnimallee 14, 14195 Berlin, Germany. E-mail: nikolaus.schwentner@physik.fu-berlin.de

^b Institut für Mathematik II, Freie Universität Berlin, Arnimallee 2–6, 14195 Berlin, Germany

Received 30th January 2004, Accepted 6th April 2004

First published as an Advance Article on the web 12th May 2004

Photodynamics calculations of a ClF molecule in solid Ar are compared to experimental results and a new interpretation is given for the observed femtosecond-pump-probe signal modulation. We analyze the round-trip and depolarization times for the excited state wave-packet motion and discuss the incorporation of lattice cage motions that partially explain the time dependence of the measured signal. Librational eigenstates and eigenenergies are calculated by solving the rotational Schrödinger equation in the previously computed [T. Kiljunen, M. Bargheer, M. Gühr and N. Schwentner, *Phys. Chem. Chem. Phys.*, 2004, **6**, 2185–2197] octahedral potentials that hinder free molecular rotation in the solids. The obtained level structure is compared to infrared-spectroscopic results. We comment on the correspondence between temperature effects in the classical dynamics of the nuclei and the quantum mechanical probability distributions. We find the combinative treatment of different simulation temperatures congruous for interpreting the experimental results at cryogenic conditions.

I. Introduction

In the previous article,¹ we sketched the outcome of the molecular dynamics (MD) calculations on the substitutional impurity molecule ClF in Ar and Kr host lattices. The computational method was described in that paper. The validity of the method was dictated by the choice of the input parameters for pair-potential evaluation, and the construct of the multidimensional potential energy surfaces in terms of the approximative diatomics-in-molecules (DIM) scheme. The classical treatment of propagation of the nuclei also clearly affected the dynamics of the system. In addition, neglect of nonadiabatic transitions and inability to treat charge-transfer reactions as the F atom was shuttling between Cl and rare gas (Rg) atoms were the limitations of the adopted method. Quantum effects were artificially mimicked by three means: varying the simulation temperature, using a probabilistic pump-excitation scheme, and by abrupt potential changes from the initially excited $^1\Pi_1$ to the $^3\Pi_0$ state of the molecule. We evaluated the computational observables thoroughly in the paper. In particular, we could find the preferential molecular orientations and their temperature dependence in the solids as a highly sensitive probe for the utilized potentials. These initial conditions were of chief importance in determining the temporal properties of the trajectory ensembles on the excited states. In other words, the photodynamics resulted from the ground state properties to a large extent, and proved the classical single-potential description to be suitable for a qualitative study of the ClF/Ar system.

The first part of the study¹ comprises a standard computational approach for a treatment of an impurity molecule in a solid. Without experimental information, the investigation would have been completed there. Taking the experiment² now into account, we need to match the observations together and further analyze the results. Key observables that we discuss here with experimental comparison are: (i) the time structure of

nuclear wave-packet motion on the excited potential energy surfaces, (ii) the change of molecular angle distribution during the dynamics, (iii) the relaxation of excess energy, and (iv) the response effects of the solid surroundings. Weight is given to discussion of the role of temperature in the classical description of these microscopic events.

We emphasize that knowing the ground state molecular orientation with respect to the solid cage is very important, for instance, when analyzing the experimental spectra or designing quantum mechanical calculations capable of treating only few degrees of freedom.^{3,4} We know from atomic radii and lattice constant considerations that the ClF molecule occupies a single substitutional site in the fcc crystal. We sketch our recent findings¹ of the preferred ground state orientation toward (or alignment in the direction of) the tetraatomic window consisting of nearest neighbour Ar atoms, and the resulting different cage-induced dynamical effects in Fig. 1. After the dissociative photoexcitation, the predominant feature is that the fluorine exits the cage through the tetraatomic window, then collides with the second shell atom, and recombines with the Cl inside the cage (trajectory A). Other directions in the cage (due to the width of the angle distribution) at the moment of the pump excitation lead to collision-induced reorientations of the molecule and to diverse bond length oscillations ($r_{\text{Cl-F}}(t)$ of trajectory B). Direct cage exit and permanent dissociation is possible through the triatomic window (with >0.8 eV excess energy), but this (trajectory C) is a rare event in the simulations.¹

Previously, the initial orientation of a diatomic halogen in a solid Rg has been considered as follows: First of all, double substitutional cases such as Cl₂/Ar, Br₂/(Ar,Kr) or I₂/Kr (ref. 2) are trivial, since two nearest neighbour lattice positions are occupied by the halogens and a cylindrical trapping cage then forms fixing the orientation. The relevant cases for comparison with the single substitutional ClF/(Ar,Kr) system are Cl₂/Xe and F₂/(Ar,Kr). The Cl₂/Xe system was studied by Gersonde and Gabriel,⁵ and by Alimi *et al.*⁶ Minimum energy orientation in the crystal was found to favor the $\langle 110 \rangle$ direction

[†] Present address: Max-Born-Institute, Max-Born-Strasse 2A, D-12489 Berlin, Germany

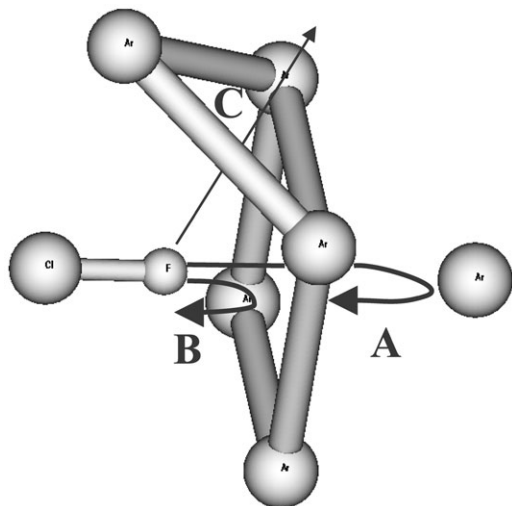


Fig. 1 Portion of the Ar cage in the direction of the CIF molecule axis, showing the three characteristic orientations: toward the tri- or tetraatomic window or toward nearest neighbour lattice atom. Preorientation in tetraatomic window (A) leads to long-range dynamics on the excited state, several oscillations with $r_{\text{Cl-F}}$ reaching over 3 Å and >250 fs round-trip periods. Triatomic window (C) is dissociative but rarely occupied. Collisions to the cage wall of nearest neighbours (B) lead to molecular angle-scattering motion and incoherent time structure in the pump-probe signal.

(nearest neighbour) over $\langle 100 \rangle$ (tetraatomic window) because of the dominating linear Xe—Cl₂—Xe configuration and relative tightness of the tetraatomic window due to Cl-Xe repulsions. Our CIF/Kr case¹ coincides with this result since there the nearest-neighbour direction gives the energy minimum due to strong halogen-Kr V_{Σ} pair interactions, and in both Ar and Kr the tetraatomic window sterically inhibits the cage exit of the Cl fragment. For F₂/(Ar,Kr) an inverse temperature dependent dissociation probability was experimentally observed and attributed to locked prealignment of the molecule along “reactive cones” of the cage at low temperatures (4 K).⁷ The early MD simulation of F₂/Ar reports $\pm 12^\circ$ deviation from the tetraatomic window ($\theta = 0$) at 4 K, by analogy with Fig. 1, and shows free rotor properties at 12 K.⁸ The temperature dependence of the dissociation quantum yield was reproduced by the simulation. The reactive cones were identified as indirect ($\theta = 10^\circ$, near the tetraatomic window) and direct ($\theta \approx 54^\circ$, triatomic window) channels for the F atom migration into interstitial O_h trapping sites. Even though the triatomic window centre was not populated at the lower temperatures, these studies provide the source for the current usage of $\langle 111 \rangle$ direction (triatomic window) as a starting point in recent simulations of permanent photodissociation.^{3,4} Due to qualitatively different results dictated by Cl-Rg and F-Rg interactions, it is not *a priori* clear which orientation dominates the CIF case, and the balance between formation of minima in tri- or tetraatomic windows was found to be delicate in Ar.¹

The experimental scheme of pump-probe spectroscopy relevant to this study is presented in Fig. 2. The pump pulse prepares a wave packet from a coherent superposition of levels in the excited electronic state B $^3\Pi_0$ or $^1\Pi_1$ above the gas phase dissociation limit. It should be noted that these continuum states become matrix-bound to vibrations due to the external potential. The probe pulse promotes the evolving wave packet to the final state E, when the wave packet is within the probe window range and the resonance condition ($E_E - E_B = h\nu_{\text{probe}}$) is fulfilled.⁹ After nonradiative relaxation within the charge-transfer manifold, the fluorescence from the D' state is detected.¹⁰ Interpretation of this time-dependent signal with help of the classical MD simulations is our goal in the present study.

In a Kr matrix, unfortunately, no pump-probe induced fluorescence signal directly from the parent Cl⁺F⁻ molecular

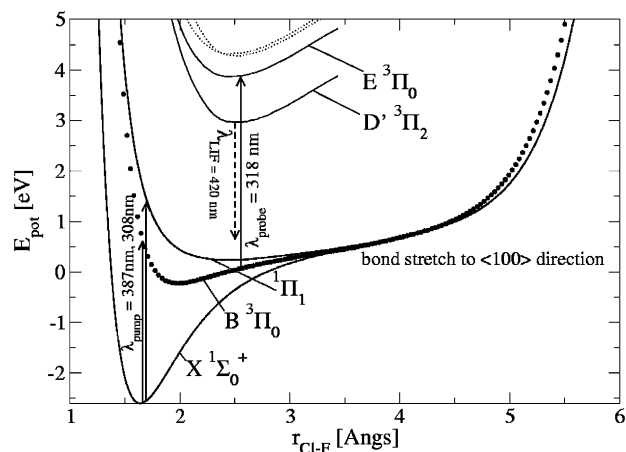


Fig. 2 The CIF potential energy curves $V(r_{\text{Cl-F}})$ in fcc Ar (lattice constant 5.3125 Å) for the ground ($X \ ^1\Sigma_0^+$) and excited states (B $^3\Pi_0$, $^1\Pi_1$). The molecule points to a tetraatomic window and during the bond stretch the center of mass is fixed at the thermalized equilibrium position¹ 0.2 Å from the substitutional site. The red-shifted ionic pump-probe target (E) and emitting (D') states are sketched roughly by the indicated curves and their gas phase values are plotted with broken lines. The arrows locate the centers of pump and probe resonance window ranges.

state (D') ($\lambda_{\text{LIF}} = 420$ nm in Ar) has been observed.^{11,12} Instead, only the exciplex emission of Kr₂⁺F⁻ prevails,^{11,12} and consequently no direct comparison of the dynamics calculations to the experiment is available. While not treated further in the present article, we comment the Kr case here as follows: The trajectories¹ in Kr did not show the expected 50% dissociation quantum yield found in the A' state fluorescence bleaching study.¹⁰ Local melting might be argued on the experimental side for such high exit probability in long illuminations of the bleaching studies, but the femtosecond study of Kr₂⁺F⁻ fluorescence,¹¹ originating from F atoms which have left the cage, shows clearly the parent molecular oscillations and rapid rise of the signal. In principle, the present simulations should have been able to reproduce this, unless the dissociation over ion-pair states excited by two-photon transitions is responsible for a large fraction as was argued in ref. 11. When we forced the alignment into a triatomic Kr window ($\langle 111 \rangle$ direction, presupposed to be dissociative) the dissociation turned out once more to be completely prevented in the simulation.

In this paper, we begin in Section II with discussion of the above observations (i)–(iv) for CIF in Ar, and find apparent contradictions between experimental pump-probe signal and the computed photodynamics. This comparison is presented in Section IIIA. As a consequence we suggest a novel interpretation of the experiments to bring the results to the same footing in Section IIIB. In order to quantify the zero-point effect for the molecular rotational motion in the solid, we calculate the librational wavefunctions in Section IIIB. The stationary states in the rotational potential in turn reveal the effective barrier heights important for the possibility to align the molecule by a nonresonant electric field. Validity of the used symmetrical potential is discussed in connection with experimental infrared data shown in Section IIIB.

II. Photodynamics

A. Comparison of experiment and theory

We recorded¹ the CIF trajectories for two types of excitations, with 0.6 eV and 1.4 eV excess energies, and construct here the pump-probe spectra by simply counting the trajectory passages through the probe window position. This is fixed by the resonance condition between the valence state B and the charge-transfer state E at $r_{\text{Cl-F}} = (2.55 \pm 0.06)$ Å, the 0.12 Å range originating from the energetic width of the fs-laser pulse.

The experimental signals² consist of pump-excitations from the ground state ($\lambda_{\text{pump}}=387$ nm/280 nm for $^3\Pi_0/{}^1\Pi_1$), time-delayed probing of the evolving wave packet from the B $^3\Pi_0$ state ($\lambda_{\text{probe}}=318$ nm) and detecting the resulting Cl^+F^- charge-transfer state fluorescence at $\lambda_{\text{LIF}}=420$ nm. The direction of the probe field linear polarization was varied with respect to the pump field. The fields were set either parallel (\parallel) or perpendicular (\perp) to each other in the $\lambda_{\text{pump}}=387$ nm case, and only perpendicular for the higher energy case. In the simulations, we recorded the direction cosines of the molecular axis with respect to the laboratory frame. We exploit this information with the r_{CIF} trajectory data and obtain the polarization dependent signal intensities by multiplying the resonance counts by

$$I_{\parallel,\perp}(t) = \sum_i^n \int_0^\pi \sin\theta_e d\theta_e \times \int_0^{2\pi} d\phi_e \underbrace{\cos^2\theta_{ei}(0)}_{\text{pump}} \underbrace{\cos^2\theta'_{ei}(t)}_{\text{probe}}. \quad (1)$$

The angle θ_{ei} between the pump field polarization and the molecular axis of i^{th} trajectory is written in terms of the spherical integration variables (θ_e, ϕ_e) and the direction cosines. The angle θ'_{ei} applies for the probe field accordingly. For the parallel pump-probe set-up, $\theta'_e = \theta_e$ and $\phi'_e = \phi_e$, whereas in the perpendicular case $\theta'_e = \theta_e + \pi/2$, $\phi'_e = \phi_e$ for one component (I_{\perp}) and $\theta'_e = \pi/2$, $\phi'_e = \phi_e + \pi/2$ for the other ($I_{\perp'}$). The integration accounts for the isotropy of the polycrystalline sample conditions in the experiment. The above applies for the $\Delta\Omega = 0$ transition to the B $^3\Pi_0$ state, whereas for the ${}^1\Pi_1 \leftarrow \text{X } {}^1\Sigma_0^+$ case we use instead a $\sin^2\theta_{ei}(0)$ pump selection^{13,14} in eqn. (1).

We present the pump-probe spectra in Fig. 3. While no serious attempt is made to construct a signal by convoluting appropriate optical field profiles with the trajectory ensemble (see, e.g., refs. 15 and 16), we note that the effects are indirectly accounted for. First, the probabilistic excitation condition in the simulation already treats the spatial distribution of the

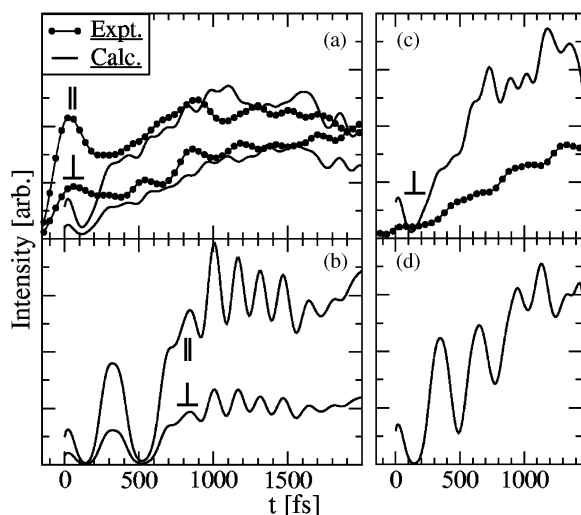


Fig. 3 (a,b) Synthesized pump-probe signals are drawn by solid curves for $\lambda_{\text{pump}} = 387$ nm to ${}^3\Pi_0$ excitation ($\Delta\Omega = 0$ transition B \leftarrow X) for CIF in Ar at 5 K (b) and at 46 K (a) simulation temperatures. The experimental signals for this transition (the curves with spherical symbols), measured at 5 K, are given together with the spectra simulated at the higher temperature (a). The two experimental spectra in (a) were recorded pump (387 nm) and probe (318 nm) field polarizations parallel (\parallel) or perpendicular (\perp) to each other, the higher intensity corresponding to the \parallel -case. (c,d) Signals for $\lambda_{\text{pump}}=308$ nm to ${}^1\Pi_1$ excitation ($\Delta\Omega = 1$) at 5 K (d) and at 46 K (c). The calculated signals are generated according to eqn. (1), and only the \perp -component is shown. The corresponding experimental signal in (c) is of equal intensity to those in panel (a) at ca. 2 ps.

pump window by encoding the range into trajectories. Second, the definition of constant probe window location with 0.12 Å width broadens the signal on the other part. The temporal distribution is only introduced *ad hoc* by replacing the counted occurrences of the trajectories in the probe window range by a Gaussian having a FWHM of 100 fs. This is just broad enough to merge the inward-outward movement of the first wave-packet oscillation feature in the signal, and is convenient for the interpretation given below.

The generated spectra with $T = 5$ K and $T = 46$ K conditions are drawn in the lower and upper panels, respectively, of Fig. 3. The first calculated peak at 30 fs results from probing the highly energetic wave packet in outward motion due to repulsive CIF interaction (*cf.* Fig. 2). In the case of $\lambda_{\text{pump}}=387$ nm and $T = 5$ K, panel (b) in Fig. 3, the F fragment penetrates the tetraatomic window, collides subsequently with a next shell Ar, and returns inside the cage. Meanwhile, the Cl fragment opens its tetraatomic window, without a breakthrough, and returns near to the substitutional vacancy in the cage. This process is relatively slow and the fragments meet at 330 fs, in the middle of the first in-out signal peak. Here, the probe pulse catches the coherent wave packet twice at the bound part of the B-state potential with ca. 100 fs separation, first moving inward (recombining) and then outward (dissociative). This is too fast to be resolved. The second oscillation is similar, with the in-out peak centered at 740 fs, whereas the later periods are shorter and happen within the cage. This gives the pronounced 160 fs modulation to the signal at 5 K. After 1.5 ps the synthesized signal becomes noisier. Quite the same is found for the $\lambda_{\text{pump}} = 308$ nm at 5 K case, panel (d) in the figure, where two distinguished oscillations are seen at 350 fs and 660 fs before blurring of the signal. We note that the first peak at 30 fs in this excitation case is naturally not detectable in the experiment, since all population is yet in the initially prepared ${}^1\Pi_1$ state but only B-state population is probed to the E state with the 318 nm pulse. The higher temperature leads to less structured signal in both excitation cases, (a,b) and (c,d) of Fig. 3, due to the incoherence of the wave packets. Together with the synthesized spectra, we reproduce the experimental femtosecond pump-probe signals. As seen in the upper left panel (a) of the figure, the parallel configuration gives higher intensity ($I_{\parallel}/I_{\perp} = 3$ directly after excitation at $t=0$) as expected due to the different photo-selections. This polarization dependency of the pump-probe setup geometry is seen to vanish at 2 ps. The experimental signal intensities in both (a) and (c) panels are scaled equally, so that the spin-flip (${}^1\Pi_1 \rightarrow {}^3\Pi_0$)^{17,18} and depolarization² times can be deduced. For the former analysis, a magic angle setup between the \parallel and \perp configurations was actually used.

With the probe wavelength that scratches the B-state wave packet near the asymptote of the bound region, a pattern of three clear oscillations was experimentally resolved at 5 K, and approximately 10% signal-modulation depths were reached (panel (a) of Fig. 3). This is closer to the 46 K simulation result, and we mark this as a discrepancy (I). The perpendicular measurement setup, which is especially sensitive to molecules that are tilted 90° with respect to the pump geometry, shows the wave-packet structure between 300 and 900 fs somewhat better resolved. The oscillations are superimposed on a rising background signal due to the wave-packet dispersion and scattering by the matrix. The synthesized signal features clearly underline faster dynamics with respect to the experiment, where a first round-trip time of ca. 600 fs was extracted¹² and the further broad signal oscillations show 300–350 fs periods. With this interpretation the simulated wave-packet motion seems too fast by a factor of two, as we have for the long-range out-of-the-cage dynamics an approximate time scale of 300 fs, which is then followed by the in-cage 160 fs oscillations. This division into long and short time periods leads to an additional discrepancy (II), since the long-range oscillation occurs twice in the simulations. As a hint for the

cure we mention that the pronounced dip in the experimental spectra at 300 fs can be attributed to the breathing motion of the cage atoms^{1,12} (*cf.* inset of Fig. 6, later).

The fast time structure giving a fingerprint of the coherent wave-packet oscillation is lost when probing deeper in the potential well.¹² On the theoretical side, shortening the probe position from the chosen 2.55 Å (318 nm) results in decrease of the 160 fs modulation depth. Setting the probe window farther, $r_{\text{CIF}} > 2.8$ Å, the signal is lost after three oscillations due to energy relaxation, whereas in the experiment the signal fades out at 10 ps with 318 nm probe. The 2.55 Å window position thus yields results in agreement with respect to the signal envelope of the experiment. The vibrational energy relaxation was estimated from the probe-wavelength dependent rising times of the maximal pump-probe signal intensity,¹² showing extensive (80 %) initial dissipation followed by a slow regime in bound region of the B-state potential. The classical molecular dynamics agrees on this part by showing that all the excess energy is lost during the first collision. We extract the relaxation rates from the time-dependent CIF kinetic and potential energy averages shown in the previous article.¹ The early decay amounts to 0.4–0.5 eV ps⁻¹, when deduced after several oscillations at 1.7 ps, which is the experimental¹² signal maximum time τ_m . The slow regime is difficult to assess due to the short simulation time and the noisiness, and merely a rough estimate of few hundred wavenumbers per picosecond can be obtained.

The recorded turning of the molecular angle after the computed pump excitation is here interpreted in terms of depolarization effect that was observed in the experiments. The depolarization of the excited molecular ensemble can be extracted from the angle changes after the excitation. This is done directly from the calculated polarization dependent signals of eqn. (1) with the anisotropy formula

$$R(t) = \frac{I_{\parallel}(t) - I_{\perp}(t)}{I_{\parallel}(t) + 2I_{\perp}(t)}. \quad (2)$$

The two \perp -components of eqn. (1) were averaged prior to inserting into eqn. (2). The result for 387 nm excitation is shown in Fig. 4. The 46 K simulation represents the closest case with respect to the experimental rapid decay, which however was measured at 5 K. The simulated 5 K case maintains the molecular orientation also after energy relaxation to the bound part of the potential in contradiction (III) to the experiment.

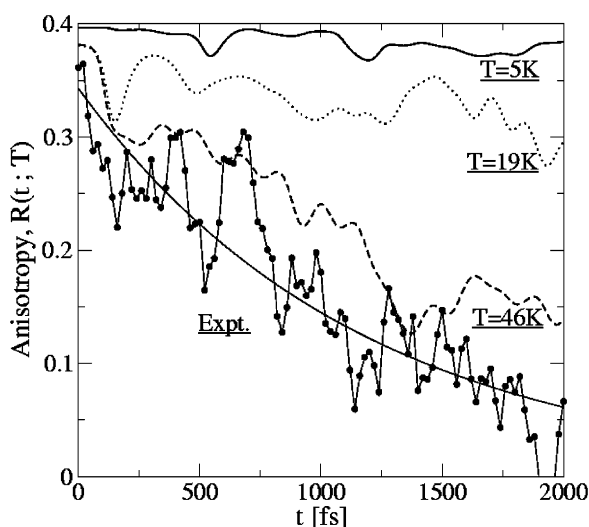


Fig. 4 The anisotropy R of CIF in Ar, obtained from the angle changes by eqns. (1) and (2) for 387 nm pump excitation at the three temperatures (solid, dotted and dashed lines). The experimental result (spherical symbols) with its exponential fit (solid) shows the fastest anisotropy decay.

Experimentally, the depolarization time $\tau_r = 1.2$ ps was obtained from the fitting curve at $R(\tau_r) = R(t=0)/e$. We note that the linearly polarized pump pulse picks a $\cos^2\theta$ distributed molecular ensemble¹³ and the probe pulse parallel or perpendicular to it further selects the same population lobe, which give the scale for the depolarization measure ($R = 0.4$ at the beginning).

B. Consequences

Although the actual shapes of the general signal features are rather arbitrary with the present account of pulse time-profiles, the distinct peak structure at 300–400 fs which is nearly *absent* in the experiments requires further thought. It has been already suggested^{11,19} as a possible explanation, that the probe window is lost in the experiment due to large dislocation of the window atoms upon the first bond stretch and corresponding blue-shift of the charge-transfer E state with respect to the solvated molecule. This is grounded on the observation of 4500 cm⁻¹ solvation red shift¹⁰ (*cf.* Fig. 2) and the fact that the 318 nm probe is just at the limit of reaching the E state at favorable solvated configuration.¹² We note that already 0.5% variation of trapping cavity diameter, produced by a coherent zone boundary phonon with an amplitude of 0.02 Å, was found to modulate the pump-probe signal intensity by 10% in a recent study of I₂ in Kr.²⁰ Here, considering the >0.5 Å atomic dislocation,¹ the reduction of solvation due to expanded cage is most effective and may very well shift the probe target potential out of the accessed energy range.

As shown in the previous article,¹ by time-dependent dislocations of the most energetic rare gas atoms and their radial distribution functions (RDF), the maximum of the lattice cage expansion coincides with the 300–400 fs molecular oscillation (reproduced in the inset of Fig. 6). The Ar cage opening is due to the impulsive kick²¹ upon change of the molecular state (anisotropic change of the electron density) and subsequent motions driven by the oscillating molecule. As for the pump-probe detection sensitivity, the RDF peak shift in Ar indicates expansion of the first coordination shell. The surrounding shell is not relaxed within the simulation running time as the breathing dislocations continue to take place. This continues the signal modulation by shifting the probe window in time. The pair-correlation functions $g_2(r;t)$ of the previous study showed that the first molecular round-trip is responsible for the major changes in the lattice. The amplitude of later cage-openings is much reduced and affects the solvation less. In Kr no deviation from ground state RDF was really seen as the head-on collision merely shifts two atoms out of the twelve nearest neighbours initially, while in Ar this ratio is close to 8:12 and the potential shift is pronounced. In the simulation, the signal intensity is due to the spread of the wave packet and its velocity in the resonance window. Therefore, the signal is so intense at later times with respect to the first bond stretch. In the experiment, however, this rise is counterbalanced by the potential shifting that modifies the probe transition probability, and the initial peak endures very distinct in the spectrum.

Therefore, for the first *ca.* 500 fs, the experiment and theory are brought into agreement by stating that the first in-out wave-packet oscillation in the experiment is nearly invisible due to the reduced solvation shift of the charge-transfer target potential. A feature of that motion is seen in the perpendicular spectrum in Fig. 3. The shift is more effective for the parallel-probed molecular ensemble which is predominantly maintained in the tetraatomic window direction than for the perpendicular case, as the \perp -probe excites contributions with tilted orientations with respect to linear pump polarization. This signal emerges from molecules prone to scattering events which cause somewhat less effective initial opening of the window. The window opening partially solves the discrepancy (II), for the 600 fs round-trip hypothesis can be excluded.

Later on, the experimental spectrum continues to show 300–350 fs periodicity for *ca.* 1 ps. According to the calculations, this must correspond to well-oriented molecular case with oscillations through the tetraatomic window. In the shown trajectories, however, this motion continues only for two periods (II). We attribute the shorter 160 fs oscillations to later dynamics in the experiment, when the signal modulation is no more resolved. The faster dynamics also corresponds to angle scattering events, direct collisions to the nearest neighbour atoms, which is completed in terms of anisotropy decay within 2 ps. The scattering part of the molecular ensemble gives less contribution to the periodic modulation of the pump–probe signal but corresponds to signal background rise of both parallel and perpendicular measurements (I,III). Even though the energy loss during the first encounters of the molecular fragments with the cage atoms is very large, the recombining wave packet remains coherent, if the molecule is aligned in a tetraatomic window. The resulting signal modulation even after the large energy losses, in both parallel and perpendicular pump–probe schemes, indicates that the collisions can maintain the coherence in these dissipative systems.²²

Support for the interpretation comes from depolarization analysis. We know from the experiment that not all the molecules in the excited ensemble point strictly to a tetraatomic window. This is partially due to $\cos^2\theta$ -dependent distribution and partially due to width of preferred initial orientation in the cage. The simulation with artificial Debye-guided $T'(\theta_D) = 46$ K temperature,¹ that by sampling the wings of the quantum librational distribution more likely leads to molecule axis pointing to nearest neighbour directions at the moment of excitation, gives the collision-induced angle-scattering time-scale correctly. In order to get the fingerprint of coherent wave-packet oscillations resolvable, the localized distribution at 5 K has to be used in simulation. Thereby we understand the origin for the points (I) and (III) made above. The difference remains in the number of long-range oscillations into and out of the cage, two compared to 3–4 (noisy) occurrences in experiment. We note that the potential energy landscape of the molecule is highly sensitive to small changes of Ar atom distances, which supposedly affects the probability for successive cage-exit motion.

Cross sections of the potential energy surfaces¹ $V(\theta, \phi)$ exemplify in Fig. 5 the librational degree of freedom of the molecule and its dependence on the lattice constant. The cuts $V(\theta; \phi)$ are performed, first, for a static fixed lattice (*cf.* Fig. 2 of ref. 1), and second, so that the matrix atom positions as well as the CIF center of mass are relaxed for every orientation $\theta = [0^\circ, 90^\circ]$ of the molecule. The geometry-optimized parts in the figure confirm the observations that the tetraatomic window orientations are preferred and the bond rotations occur through nearest neighbour directions in the cage. The solid horizontal lines in Fig. 5 indicate the two discrete eigenlevels that we find later in the article for the static lattice case (*cf.* Section IIIA). Without knowing the librational zero-point energies and level structures in these potentials, assumptions on the angular distributions that could guide classical simulations are not well grounded. For instance, a weighting function of type $\exp(-V/k_B T)$ may be introduced to sample a ground state quantum mechanical probability density, provided that the potential V is known. Here, however, the experimental result of depolarization implies that this is not applicable. Putting the guided distribution on the ground state in Fig. 5(b) would lead to an angular width too narrow to yield the depolarization dynamics observed. In order to simulate this experiment, we used the temperature scaling method to provide an appropriate angular width in the initial distribution $\rho(\theta, \phi)$.¹ The guided distribution could be considered justifiable *a posteriori* for an initial value representation of the angular distribution in the tight lattice with the steep potentials. However, in the high temperature case of panel (b), population in

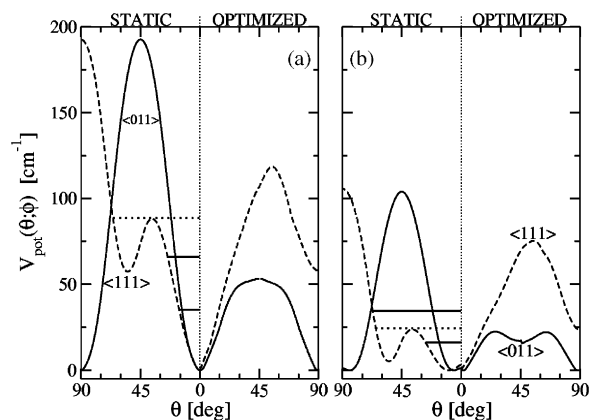


Fig. 5 Potential energy cuts $V(\theta; \phi)$ for the CIF rotation in the Ar cage. In panel (a) we plot the tight surrounding case with the Ar lattice constant of 5.224 Å (corresponding to the zero pressure constraint at 5 K)¹. The right-hand panel (b) shows the looser matrix with 5.301 Å lattice constant (46 K). The solid curves show the dependence of the potentials on the polar angle θ with ϕ fixed to 0° , *i.e.*, the orientation changing from one tetraatomic window at $\theta = 0^\circ$ to another through the nearest neighbour direction $\langle 011 \rangle$. The dashed curves represent a cut with $\phi = 45^\circ$, *i.e.*, from $\langle 001 \rangle$ through $\langle 111 \rangle$ to $\langle 110 \rangle$. In both panels, the left half shows the result in a fixed lattice (static), whereas in the right half the geometry was optimized for every orientation of the molecule. The horizontal lines locate the static barriers (dotted) and indicate the discrete librational levels (solid) in this case (*cf.* Fig. 7).

the second level above the barrier is no more negligible according to Boltzmann factors, and we thus rely on the classical distributions. Finally, it should be noted that the more rigorous Wigner representation of the density does not apply for the angular functions.

The quantum mechanical probability distributions, such as the ground vibrational states or the angular analog, librational states in steep rotational potential wells, are not mapped by molecular dynamics to the right extent due to accumulation on the classical turning points. Therefore, by raising the simulation temperature to account for the zero-point amplitudes of atomic displacements, the real effect is to sample more extensively the wings of the quantum wavefunction. Thus, to simulate the cold matrix-isolation conditions (4–20 K) more weight should be given to $T = 0$ K equilibrated trajectories than for higher temperatures. However, to mimic the width of the full vibrational/librational density function, different temperatures should be used and the results given in a combinative manner. We address this problem in the following. Additional test simulations showed that, if we disregard the zero-pressure constraint and use the larger lattice constant of 5.3125 Å implied by the pair-potential minimum, at 0–5 K the 387 nm excitation leads to smoother transition from long-range dynamics to in-cage oscillations. We show a specific example of new calculations in Fig. 6. Here, the simulation cube consisted of 500 lattice sites, the lattice was thermalized to 0.5 K, and the resulting internal pressure was negative, -1.6 kbar. We calculated 52 trajectories and construct the wave-packet dynamics $P(r, t)$ and the pump–probe signals as before. The result shown in Fig. 6, again plotted together with the experimental signals, gives better agreement than before for the oscillating time structure. Now, since the tetraatomic window is larger due to the lattice constant and the angle distribution is tighter, we obtain more coherent wave-packet structure with several resolvable oscillations as expected. This simulation case samples the maximum of the quantum mechanical distribution in the molecular angle space. In order to underline the idea of mixing the results of classical calculations at different temperatures, and to get the background rise of the signal in a qualitatively correct way, we actually show the spectrum in Fig. 6 *summed* from the 0.5 K and 46 K (5.301 Å lattice constant due to the pressure scaling¹) trajectories. The lattice constants in these

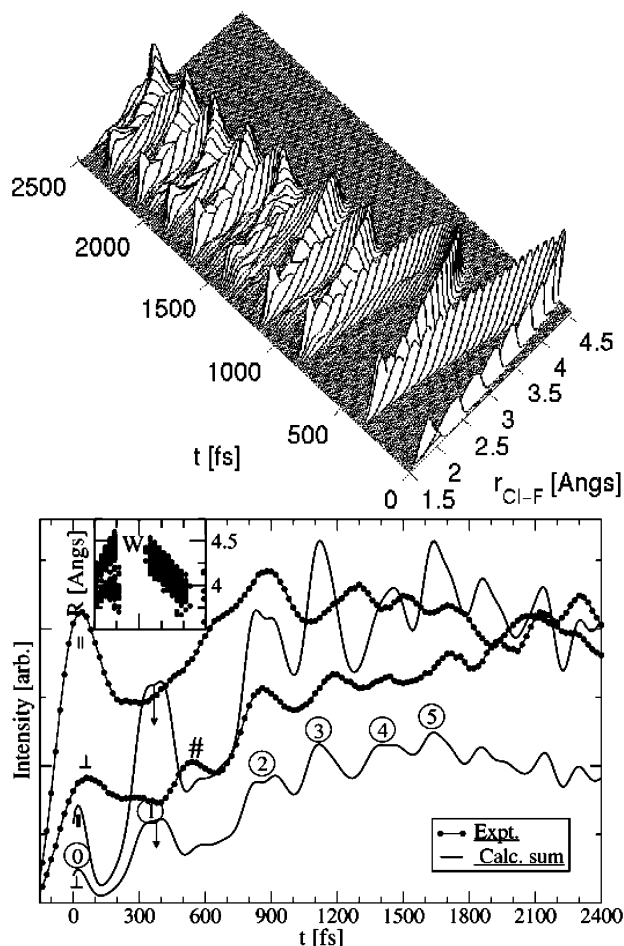


Fig. 6 Upper panel: The CIF excited state dynamics in Ar at 0.5 K presented as wave-packet construct $P(r,t)$ evolving on the ${}^3\Pi_0$ state potential after 387 nm pump excitation. Long-range dynamics ($r_{\text{Cl-F}} > 3 \text{ \AA}$) in the tetraatomic window is continued for 2 ps. Lower panel: The corresponding signal intensity when probed at $r_{\text{Cl-F}} = (2.55 \pm 0.06) \text{ \AA}$ ($\lambda_{\text{probe}} = 318 \text{ nm}$) is summed up 1:1 with the 46 K result to include the background rise. The lines with spherical symbols are the experimental pump-probe signals measured in parallel or perpendicular configuration as in Fig. 3. The numbers indicate the wave-packet round-trip periods, and the arrows locate the maximum suppression of the signal due to the lost probe resonance in the experiment. In the inset, the excited Ar atom distances R from the molecule locate the maximal expansion of the cage at W.¹

two cases were close enough for the combination of the results. Now the initial background is due to the depolarizing scattering events and the well-resolved time structure originates from the coherent part. The simplest choice for the weight, *i.e.* 1:1, is taken just to provide the idea of combinative interpretation.

Compared to the 5 K simulation with the zero-pressure constraint, the result in Fig. 6 has notable differences although it looks qualitatively the same. The long-range oscillations ($r_{\text{Cl-F}} > 3 \text{ \AA}$) can now continue for several periods and not only the first two. Also here the extent of first bond stretches are markedly pronounced but the transition to short in-cage dynamics is smoother. The generated signal in the lower part of Fig. 6 resolves the wave-packet periods up to the termination of the simulation. We read the signals as follows. The first peak (0) is the trivial outward stretch as explained above. The first in-out signal feature (1) is to a large extent absent in the experiments because the probe target state E is not reached. In the lower intensity (\perp) spectrum it nevertheless shows up slightly, because the signal originates from molecules already tilted away from the tetraatomic window and the ionic solvation shift is not so effective as for the \parallel -case. The experimental peak-feature (#) in the \perp -spectrum at 550 fs (shoulder in the

\parallel -case) appears faintly in the simulations where the tilting motion of the molecules takes place (reproduced by the 46 K case). In the experiment, also, it is expected that the initial reorientations lead to shortening of the subsequent oscillations. Alternatively, judging from the width of the first peak (0) in the experiment, the in-out (1) signal should be broader than here simulated, and therefore the rise at 550 fs may be attributed to a remainder wing of the suppressed line as the opened cage begins to relax to the new equilibrium.¹ Later, the time-scales in both the experiments and simulation give similar signal oscillations (2,3,4,5) apart from the minor shift in time.

It is notable that no dissociation takes place in simulations, in contrast to the 5% probability observed in experiment. Stating whether this is due to an inadequacy of the applied pair-potentials or the fixed orbital orientation of the atomic fragment treatment must await a nonadiabatic (full DIM) dynamics evaluation. In our align-pump-probe scheme,¹ where the bond axis was forced to the dissociative (111) window direction, the three first inner turning points were located approximately at 220, 510, and 700 fs showing that for a recombinative motion the time scales are necessarily shorter than the experiments in Ar intuitively suggested, which in part supports at least the assignment of molecular oscillation in a tetraatomic window.

III. Librations

In the classical simulations, we concerned for the zero-point amplitude of the lattice atom movements and used the different temperatures accordingly. This scaling also affects indirectly the distribution of the angular coordinate of the molecule, but as discussed above, in a statistically wrong way. For that reason, the experimental comparison was successful by factoring between different characteristic events in low and high simulation temperatures. Evaluation of the librational eigenstates in this section confirms the quantum nature of the system and connects to the validity of the angular distributions used in the dynamics simulations. Our concern about the possibility to externally align the molecular ensemble and thereby to control the photodynamics is now brought into the debate. Our classical picture gives rather high, although very sensitive, rotational potential energy surfaces that to a large extent hinder the effect of nonresonant alignment field. Here we assess the zero-point effect for the rotational motion in the shallow (with respect to vibrational) potentials. The obtained level structure and its implications are discussed with results of the infrared absorption measurement.

A. QM calculations

The computed rotational potential energy surfaces $V(\theta, \phi)$ shown in the previous article were calculated with CIF center of mass fixed at the substitutional site and the rare gas atoms occupying their perfect fcc lattice positions.¹ Because of the resulting octahedral symmetry (O_h point group), we can use symmetry adapted spherical harmonics (SASH) as a basis in calculating the librational eigenenergies and -states from the rotational Schrödinger equation. The SASH basis functions $Z_{jm}^{(\Gamma)}(\theta, \phi)$, for different irreducible O_h point-group representations (Γ) in arbitrarily high order in rotational quantum number j , are generated according to the recursive procedure of ref. 23. The use of these (real-valued) combinations of spherical harmonics Y_{jm} functions $\mathcal{Y}_{jm}^{(\Gamma)}$ greatly reduces the numerical overhead as the expansion

$$Z_{jn}^{(\Gamma)}(\theta, \phi) = \sum_{m=-j}^j c_{jnm}^{(\Gamma)} \mathcal{Y}_{jm}^{(\Gamma)}(\theta, \phi), \quad n = 0 \cdots g_{\Gamma}(j) \quad (3)$$

has vanishing components in $g_{\Gamma}(j)$, and relatively low values for j are needed for convergence in the ground electronic state.

Thus for the wavefunction,

$$\psi_k^{(\Gamma)}(\theta, \phi) = \sum_{j=0}^{\infty} \sum_{n=0}^{g_{\Gamma}(j)} d_{kn}^{(\Gamma)} Z_{jn}^{(\Gamma)}(\theta, \phi), \quad (4)$$

the number of explicitly included functions remains small. Inserting this *ansatz* into the time-independent Schrödinger equation, the problem of finding eigenvectors \mathbf{d}_k is solved by diagonalization of the Hamiltonian matrix

$$(\hat{H})_{jnj'n'}^{(\Gamma)} = Bj(j+1)\delta_{jj'}\delta_{nn'} + V_{jnj'n'}^{(\Gamma)} \quad (5)$$

where the potential energy matrix elements are obtained by numerical integration over the surface of the unit sphere:

$$V_{jnj'n'}^{(\Gamma)} = \int_0^\pi \sin\theta d\theta \int_0^{2\pi} d\phi Z_{jn}^{(\Gamma)}(\theta, \phi) V(\theta, \phi) Z_{j'n'}^{(\Gamma)}(\theta, \phi). \quad (6)$$

The eigenstates can be calculated for each irreducible representation Γ because the potential (A_{1g}) does not mix states of different symmetry. For the CIF molecule the rotational constant is $B = 0.5165 \text{ cm}^{-1}$.

We show the energy level diagram resulting from diagonalization of eqn. (5) in Fig. 7. The two rotational potential energy surfaces $V(\theta, \phi)$ dictated by the different lattice constant at 5 K and 46 K, both lead to an eigenlevel structure resembling vibrational motion, *i.e.*, we find two discrete levels followed by a state continuum. The correlation diagram in Fig. 7 shows the symmetry-wise collapse of the J_{free} -levels into librational levels. The ground state, for instance, can be represented by A_{1g} , T_{1u} , or E_g wavefunctions. For the totally symmetric A_{1g} case, the lowest level has mixed contributions from higher angular momentum basis states, significantly $j = 4, 0, 8, 6$ in decreasing order, which leads to acute angular width as shown in the inset of Fig. 7.

The different potentials, reflecting the sensitivity to the cage size, give differing energetics as a result. For instance, the level spacing $\Delta E_{1 \leftarrow 0} = 32 \text{ cm}^{-1}$ at 5 K changes to 16 cm^{-1} in the enlarged lattice. The common feature is, however, that the barrier height remains large relative to the rotational constant, and we end up with librational limit of the rotational problem. This should hold true also for a “real” potential surface, where (i) the lattice atoms are not fixed to perfect lattice positions but equilibrated around the impurity, (ii) they are mobile during the change of the molecular angle, and (iii) the CIF center of mass is allowed to move. Implications on the potential energy landscape can be seen in Fig. 5. As a combined effect of the

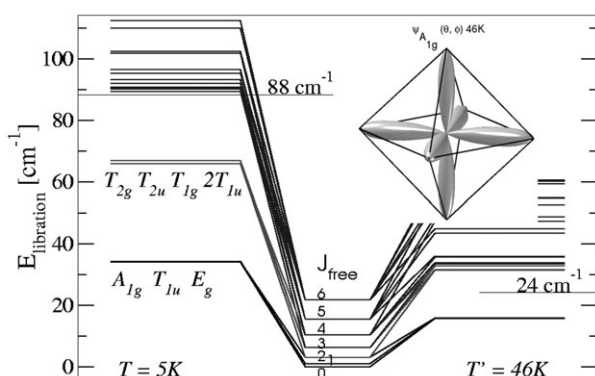


Fig. 7 The solution of eqn. (5) in the two T -dependent potentials $V(\theta, \phi)$. Librational energy levels that correlate with free rotor states up to $j = 6$ are shown. The symmetries Γ of the lowest states are indicated by their group symbols. The minimum of the potential energy surface is set to zero. Potential barrier heights, 88 cm^{-1} and 24 cm^{-1} , are also indicated. The sharp angular momentum wavefunction, $\psi_1^{(A_{1g})}(\theta, \phi)$, is inserted in the octahedron. The corners of the octahedron occupied by the wavefunction lobes point to the tetraatomic windows in the Ar lattice cage.

above, along with symmetry breaking, we expect broadening of the resulting levels. The present account of the librational problem comprises the simplest approximation, but gives a qualitative answer to the question about zero-point effects and energy-level spacings. According to the present calculation, a broadened trace of excitations to higher librational states could be expected to show up in an IR spectrum. A rough estimate locates this feature some (order of ten) wavenumbers above the fundamental transition.

The striking feature of the eigensolution is that the zero-point energy in librational regime amounts to a large portion of the potential barrier. In the present two cases of 5 K and 46 K this corresponds to $2/5$ and $2/3$ reduction of the effective potential that hinders an externally driven rotation induced by an alignment field. With this information, we can now expect that the dynamical effects modulating the barrier heights combined with the barrier-lowering librational zero-point effect, together bring the competitive energy figures closer to each other (*cf.* Fig. 5). Consequently, the high static barrier value at 5 K (88 cm^{-1}) is reduced to the same order of magnitude that can be externally imposed by a nonresonant field (damage-threshold limited 7 cm^{-1}), in contrast to the gradient approach studied in the previous article where extensive field strengths had to be used.¹ We note that considering the experimentally aimed alignment schemes, instead of mixing the free-rotor states as happens in the gas phase, here the effect of a nonresonant pulse is to create the directional hybrids out of the sharp angular momentum states in a steep rotational potential. The states calculated in the present work (Fig. 7) will act as a basis in the subsequent time-dependent alignment studies. With respect to the radial dynamics, the tight ground state rotational function obtained here corresponds closely to the low temperature simulations of the pump–probe signals. Studying further, how the actual sampling from say a linear combination of these lowest rotational eigenstates changes the simulated signal features, is beyond the scope of the present account. Nevertheless, the 46 K classical simulation is expected to produce the effect similarly.

B. IR measurements

The infrared absorption measurements for CIF in solid Ar were performed on macroscopic polycrystalline samples of approximately 3 cm^3 . The samples were grown in a plastic vessel that was attached to a closed-cycle refrigerator at a temperature of 13 K. A premixed gas of Ar and CIF was brought into the vessel. Typical pressures during the growing process were in the range of 100 mbar. The concentration of CIF in Ar was varied from $1:10^3$ to $1:10^5$. After growing the crystal, the plastic vessel was removed and the crystal was brought in the beam path of a standard FTIR spectrometer (Bruker equinox) equipped with a MCT detector. In the case of high concentrations (1:1000–1:50000) a pronounced background in the FTIR spectra shows up emerging from CIF clusters in the crystal. For both pure and doped Ar crystals, we find the damage threshold intensity $I_{\text{max}} = 0.8 \times 10^{12} \text{ W cm}^{-2}$ for the fs laser pulses at 775 nm. The vibronic spectrum shown in Fig. 8 consists of the ($\nu'' = 1 \leftarrow 0$) peak at 770 cm^{-1} accompanied with its 7 cm^{-1} ^{35}CIF – ^{37}CIF isotope shift, both on top of the broad CIF cluster background. The broad sideband assigned as arising from transitions to excited librational states (rotational fine structure) is located at $(787 \pm 10) \text{ cm}^{-1}$ and shown enlarged in the inset. Although the absorption feature observed at 787 cm^{-1} is extremely weak, its location *ca.* $(17 \pm 10) \text{ cm}^{-1}$ to the blue of fundamental transition is attractive for interpretation. Comparing to the quantum mechanical level spacings of 32 cm^{-1} and 16 cm^{-1} for 5 K and 46 K perfect lattices, respectively, we can make the assignment to librational fine structure. The broadness of the signal can be attributed to the dynamical effects smearing the discrete level structure shown in Fig. 7.

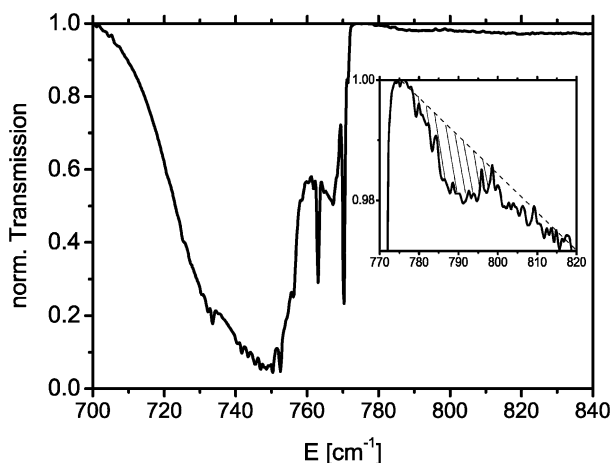


Fig. 8 The IR absorption spectrum of CIF in solid Ar. The fundamental ($1 \leftarrow 0$) vibration is located at 770 cm^{-1} (763 cm^{-1} for ^{37}CIF) and the inset shows what is assigned as librational side band centered at 787 cm^{-1} . The sample concentration was 1:20000 and growing pressure was 100 mbar. These conditions lead to the large background at lower wavenumbers.

IV. Conclusions

Experimental photodynamics² of the CIF molecule in the Ar matrix is compared to the classical molecular dynamics simulations¹ and to the generated pump–probe spectra. The ground state conditions are further assessed by quantum mechanical rotational state calculations and the infrared absorption measurement. We note as a general outcome of the research that studying temperature effects by classical MD simulations may be misleading, since instead of obtaining the result of enhanced atomic mobility the dominating effect can be due to the wrong statistical accumulation at classical turning points. Congruity can be obtained by a careful combination of the temperature dependent simulation results.

The experimentally resolvable fingerprint of wave-packet dynamics was successfully simulated using the low-temperature trajectory ensemble that is tightly oriented to the tetraatomic window of the cage. The number of the simulated long-range oscillations, where the F fragment goes through the window with larger than 300 fs period, was put in agreement with experiment by the Ar density close to the bulk value with lattice constant dictated by the Ar–Ar pair-potential. The way of obtaining correct time scales for the excited state dynamics by changing the lattice size emphasizes the sensitivity of the results on the pair-potentials. It is found that small changes in the lattice constant, due to the constraint of desired zero pressure in simulation cube, lead to tremendously different rotational potential energy barriers. However, the dynamical picture of the spontaneous reorientations on the ground state reveals¹ that tetraatomic window is the minimum energy direction for the molecule regardless of the lattice constant used. The recombinative dynamics in the tetraatomic window direction gives the time scales in agreement with the CIF-in-Ar experiments. For a triatomic window, which is found unstable for all the lattice sizes here assessed, the oscillations would be faster than experimentally observed.

The experimentally observed depolarization of the excited molecular ensemble, giving the background of the pump–probe signal without a resolved wave-packet structure, is simulated correctly by using the raised Debye-guided temperature $T'(\theta_D)$, thereby broadening the initial distribution of orientations and making the collision-induced scattering events more probable. The missing first inward-outward peak in the experiment is explained by the large dislocation of the tetraatomic window atoms upon the first oscillation. At this time, the target charge-transfer state of the probe pulse becomes less solvated and is lifted beyond reach. The perpendicular pump–probe configuration is argued less sensitive to the opening of the window and it resolves better the features of the initial dynamics.

The quantum mechanical part of the study reveals the magnitude of the librational zero-point effect in the rotational potential energy surfaces that impose high barriers with respect to the rotational constant of the molecule. The significance of the result is that the librational energy discretization leads to experimentally observed “fine structure” in IR absorption spectrum, and the high zero-point values are believed to aid the experimental alignment scheme pursued in our group.

Because the previous experiments were carried out for thin films,² we plan new measurements for CIF in large Ar crystallites (1 cm^3) to better resolve the polarization dependent dynamics. For the polycrystalline sample we should be able to find a single-crystalline environment within the laser focal size.²⁴ Following the polarization dependence in a pump–probe signal we then try to find best conditions for realizing the alignment-pump–probe scheme also. On the theoretical side, the time-dependent problem of laser-induced molecular alignment in solids is assessed in the future.

Acknowledgements

This research is supported by the project “Analysis and control of ultrafast photoinduced reactions” (SFB 450) of the Deutsche Forschungsgemeinschaft (DFG). T.K. is supported by a Marie Curie Fellowship of the European Community Programme “Improving the Human Research Potential and the Socio-Economic Knowledge Base” under contract number HPMF-CT-2002-01854.

References

- 1 T. Kiljunen, M. Bargheer, M. Gühr and Schwentner, *Phys. Chem. Chem. Phys.*, 2004, **6**, 2185.
- 2 M. Bargheer, M. Gühr and N. Schwentner, *J. Chem. Phys.*, 2002, **117**, 5.
- 3 G. Chaban, R. B. Gerber, M. V. Korolkov, J. Manz, M. Y. Niv and B. Schmidt, *J. Phys. Chem. A*, 2001, **105**, 2770.
- 4 R. B. Gerber, M. V. Korolkov, J. Manz, M. Y. Niv and B. Schmidt, *Chem. Phys. Lett.*, 2000, **327**, 76.
- 5 I. H. Gersonde and H. Gabriel, *J. Chem. Phys.*, 1993, **98**, 2094.
- 6 R. Alimi, A. Brokman and R. B. Gerber, *J. Chem. Phys.*, 1989, **91**, 1611.
- 7 H. Kunttu and V. A. Apkarian, *Chem. Phys. Lett.*, 1990, **171**, 423.
- 8 R. Alimi, R. B. Gerber and V. A. Apkarian, *J. Chem. Phys.*, 1990, **92**, 3551.
- 9 A. B. Alekseyev, H.-P. Liebermann, R. J. Buenker and D. B. Kokh, *J. Chem. Phys.*, 2000, **112**, 2274.
- 10 M. Bargheer, P. Dietrich and N. Schwentner, *J. Chem. Phys.*, 2001, **115**, 149.
- 11 M. Bargheer and N. Schwentner, *Fiz. Nizk. Temp. (Kiev)*, 2003, **29**, 225.
- 12 M. Bargheer, PhD thesis, FU-Berlin, 2002.
- 13 A. C. Albrecht, *J. Mol. Spectrosc.*, 1961, **6**, 84.
- 14 L. E. Brus, *J. Mol. Spectrosc.*, 1977, **64**, 376.
- 15 R. Zadayan, Z. Li, C. C. Martens and V. A. Apkarian, *J. Chem. Phys.*, 1994, **101**, 6648.
- 16 M. Sterling, R. Zadayan and V. A. Apkarian, *J. Chem. Phys.*, 1996, **104**, 6497.
- 17 M. Bargheer, M. Y. Niv, R. B. Gerber and N. Schwentner, *Phys. Rev. Lett.*, 2002, **89**, 108301.
- 18 M. Bargheer, R. B. Gerber, M. V. Korolkov, O. Kühn, J. Manz, M. Schröder and N. Schwentner, *Phys. Chem. Chem. Phys.*, 2002, **4**, 5554.
- 19 M. Bargheer, J. Pietzner, P. Dietrich and N. Schwentner, *J. Chem. Phys.*, 2001, **115**, 9827.
- 20 M. Gühr, M. Bargheer and N. Schwentner, *Phys. Rev. Lett.*, 2003, **91**, 85504.
- 21 S. Jimenez, M. Chergui, G. Rojas-Lorenzo and J. Rubayo-Soneira, *J. Chem. Phys.*, 2001, **114**, 5264.
- 22 M. Bargheer, M. Gühr and N. Schwentner, *Isr. J. Chem.*, 2004, , in press.
- 23 B. Schmidt and P. Žďánská, *Comput. Phys. Commun.*, 2000, **127**, 290.
- 24 W. Rudnick, R. Haensel, H. Nahme and N. Schwentner, *Phys. Status Solidi A*, 1985, **87**, 319.